Baseline VSP processing for the Violet Grove CO_2 Injection Site

Marcia L. Couëslan, Don C. Lawton, and Michael Jones*

ABSTRACT

Injection of CO_2 for enhanced recovery and sequestration purposes is increasing in Western Canada and around the world. Injected CO_2 must be monitored to in order to track its progress through the reservoir and to ensure that the CO_2 is not leaking out of the reservoir. The Violet Grove project uses time-lapse multicomponent surface and borehole seismic surveys to monitor injected CO_2. The baseline P- and PS-wave VSP data has been processed through to migration using a velocity model that was inverted for anisotropy. The VSP data images reflectors for a radius of about 200 m around the observation well. Both the P- and PS-wave images clearly tie the P-wave surface seismic while displaying improved vertical and lateral resolution over the surface seismic. The tie between the PS-wave surface seismic and PS-wave VSP image is less certain due to the poor quality of the PS-wave surface seismic.

The first monitor survey will be acquired in January 2006 and will be processed with the same parameters as those of the baseline survey. It is expected that the injected CO_2 will cause a decrease in P-wave velocities resulting in increased travel time and increases in reservoir amplitudes on the P-wave images.

INTRODUCTION

Many of Western Canada's major oil and gas fields have been depleted through primary production and secondary recovery methods. Companies are now investigating new methods, such as CO_2 flooding, to further enhance recovery. It is estimated that CO_2 flooding can increase oil recovery by 7 to 23% of the original oil in place (Bachu and Shaw, 2004). CO_2 injection for enhanced oil recovery (EOR) also has the potential benefit of CO_2 sequestration, which reduces greenhouse gas emissions into the atmosphere. Bachu and Shaw (2004) estimate that Western Canada has a practical CO_2 storage capacity of about 3.3 Gt in its oil and gas reservoirs; 450 Mt of this could be from CO_2 injected into hydrocarbon reservoirs for EOR. However, in order to claim a reduction in CO_2 emissions, the injected CO_2 must be monitored to prove that it is being trapped in these reservoirs.

Time-lapse surface seismic or borehole seismic surveys have been used to monitor injected CO_2 successfully in Encana's Weyburn Field (Li, 2003), Anadarko's Patrick Draw Field (O'Brien et al., 2004), and the Utsira Sand project in the North Sea (Skov et al., 2002). However, the cost of monitoring a CO_2 flood with repeated high resolution

* Schlumberger Canada

3D surface seismic surveys is high, and the data still may not have the bandwidth to resolve thin layers at depth. At Violet Grove, an alternative monitoring strategy has been developed consisting of sparse multicomponent surface seismic lines coupled with a borehole seismic array to provide lateral coverage of the survey area as well as high resolution images near the observation well.

BACKGROUND

The Violet Grove site, near Drayton Valley, Alberta was selected for a CO_2 EOR and storage study in conjunction with PennWest Petroleum and the Government of Alberta. The reservoir is located in the Cardium Formation in the Pembina Field. A permanent 8 level geophone array was cemented into an old production well in February 2005. The array extends from a depth of 1497 to 1640 m. The baseline seismic survey was acquired in March 2005 and consisted of two east-west source-receiver lines and one north-south source-receiver line (Figure 1). A two kilogram charge of dynamite was used as the seismic source at each shot point. The geophone array was live throughout the surface seismic acquisition and recorded three components for each shot.

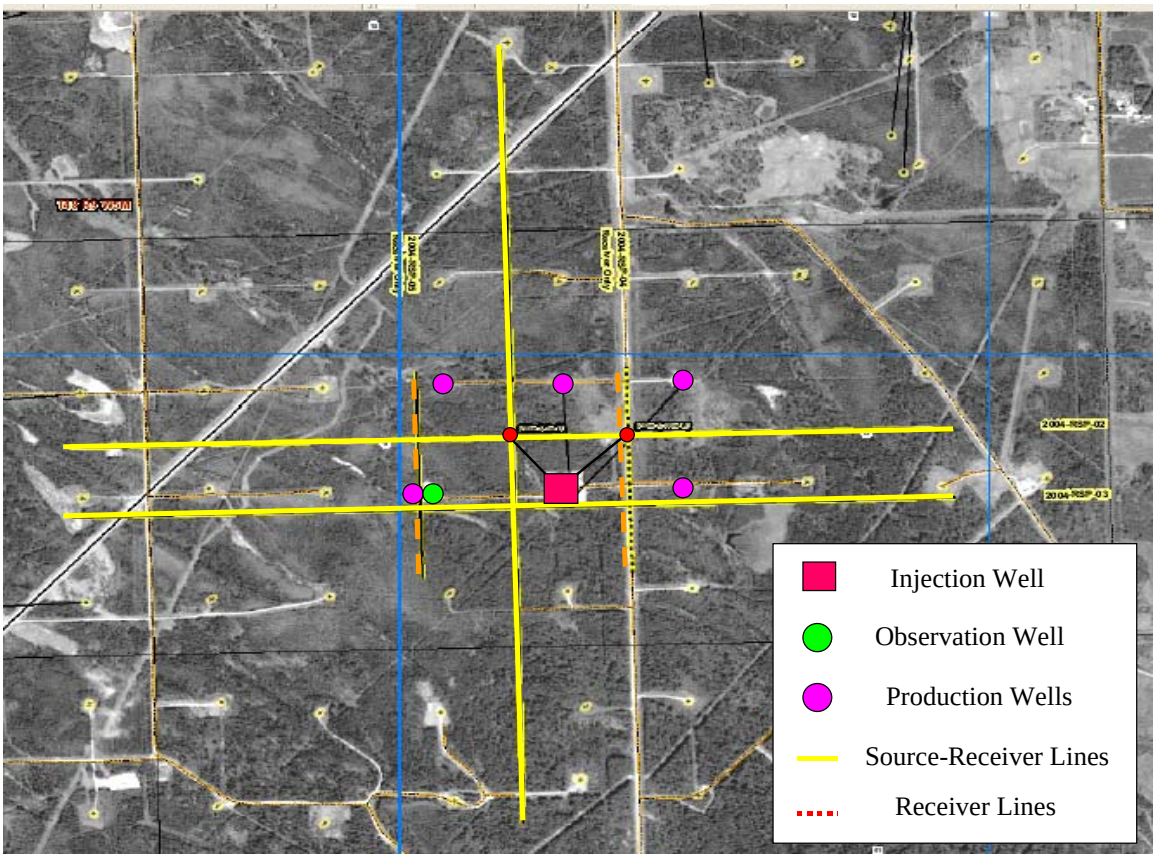

FIG. 1. Aerial photo of the Violet Grove area with annotated wells and seismic lines.

The seismic line that runs closest to the observation well was used for parameter testing (Figure 1). The VSP data was processed as three separate walkaway surveys. The S-wavefields went through the same basic processing flow as the P-wavefields. In most of the figures, the data have been sorted into receiver gathers.

PROCESSING

Processing Flow

Figure 2 illustrates the general processing flow used to process the VSP data.

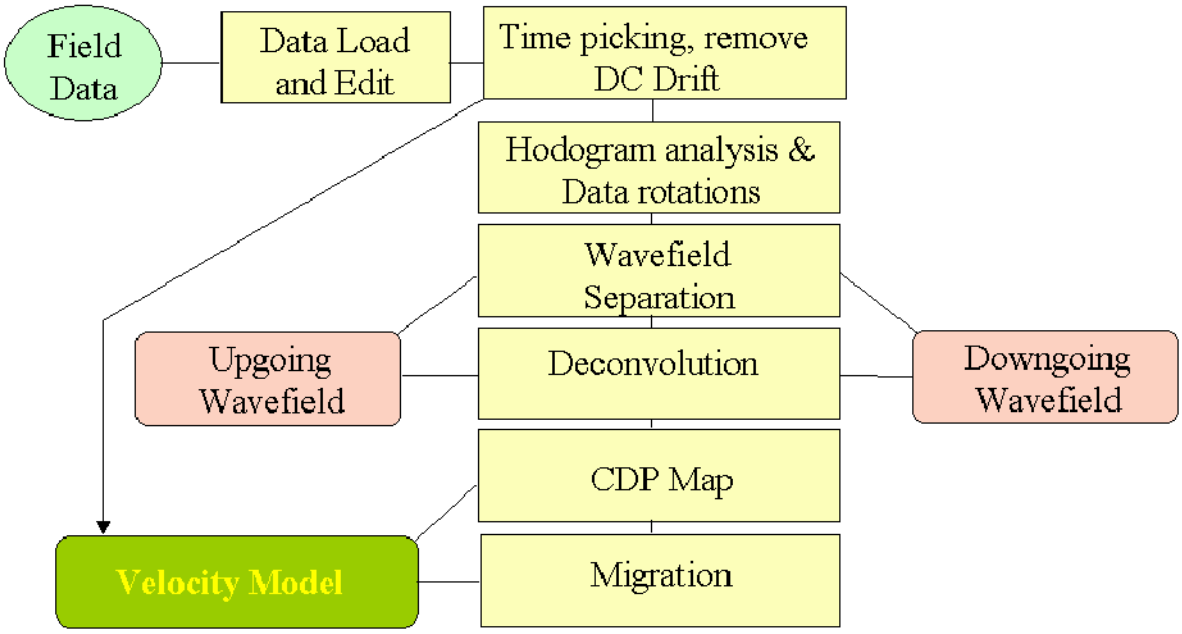

FIG. 2. VSP processing sequence.

Raw Data

Ground level in the survey area ranges between 881 and 902 m above mean sea level. A datum of 910 m was used for the surface seismic processing, so the borehole seismic data was corrected to the same datum. A low cut filter was used to remove the observed DC bias in the data. The direct arrival was picked on all three components. The raw z, y, and x components can be seen in Figures 3, 4, and 5 respectively.

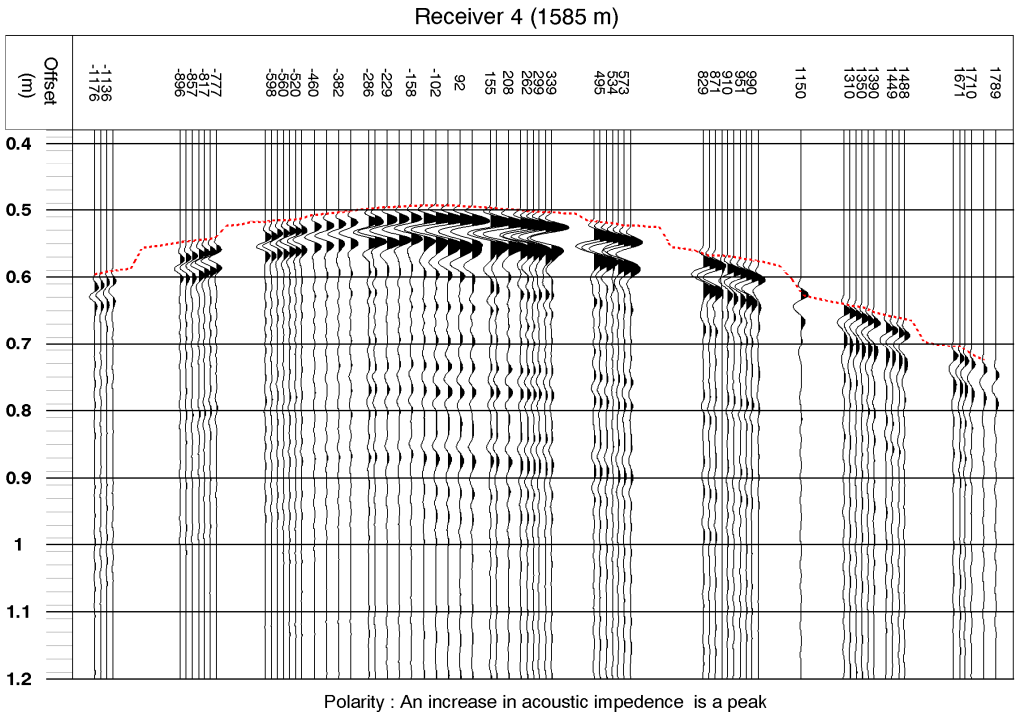

FIG. 3. Raw z component with picked first breaks.

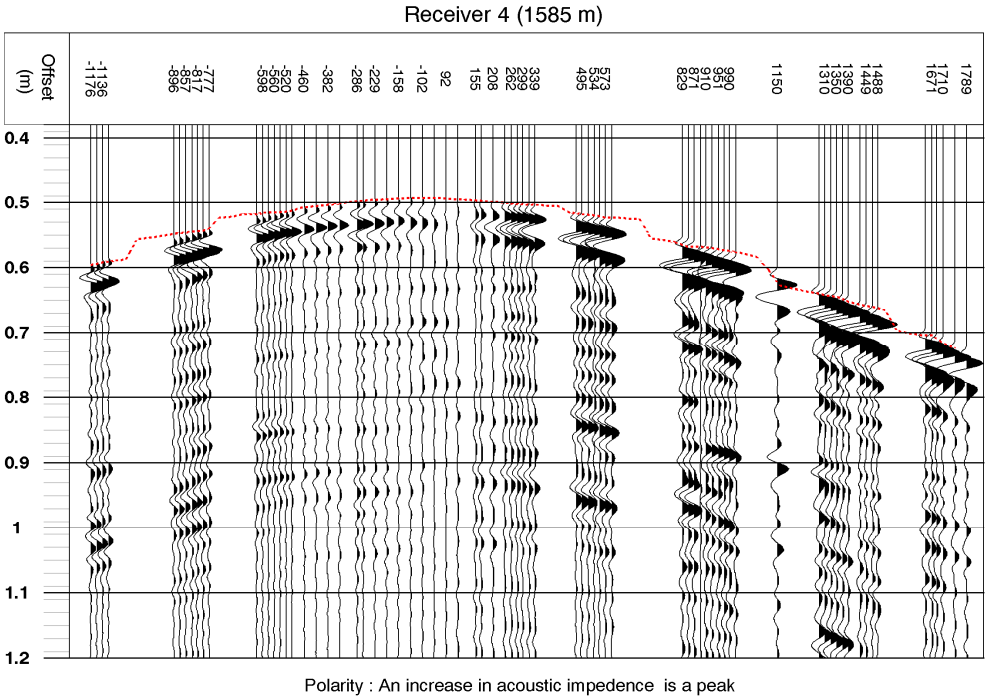

FIG. 4. Raw y component with picked first breaks.

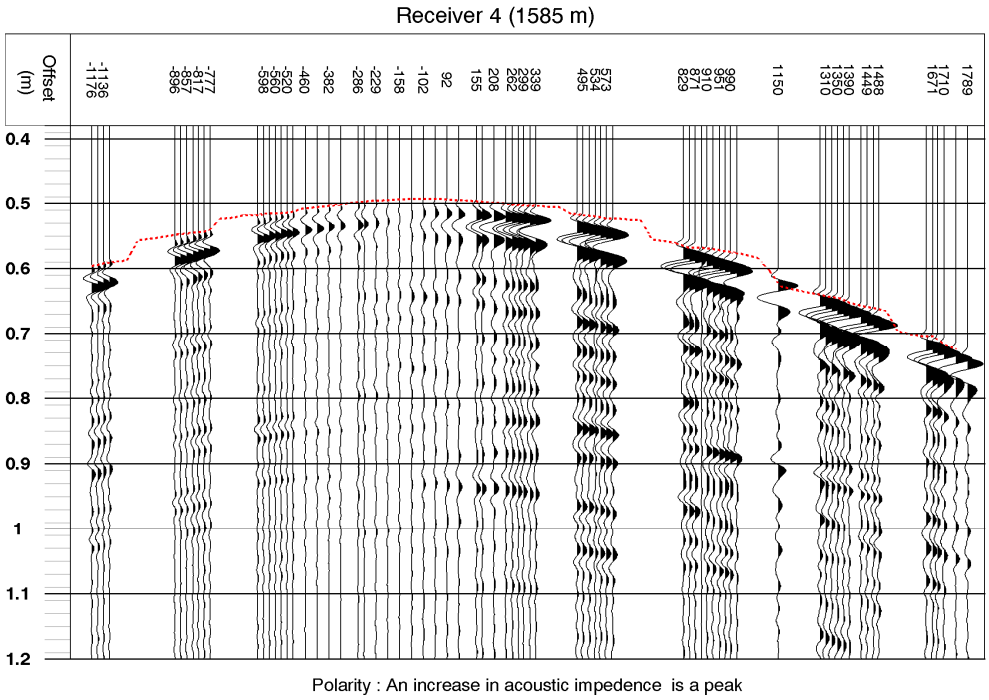

FIG. 5. Raw x component with picked first breaks.

Hodogram Analysis and Data Rotations

Hodograms analyze how the first arrival seismic energy is distributed between the z, y, and x planes in a small window around the direct arrival. In the case, the hodogram analysis used a 50 ms window around the direct arrival (Figure 6). A set of hodograms were produced and inspected for each source-receiver pair in the survey. The energy clearly fell into distinct polarizations for all offsets (Figures 6, 7, and 8). At the far offsets, energy is evenly distributed between the vertical and horizontal components (Figures 6 and 8) while the zero offset hodogram shows that the energy is found almost entirely in the vertical component of the data (Figure 7). The far offsets also indicate from which direction the horizontal component of the first arrival energy is traveling.

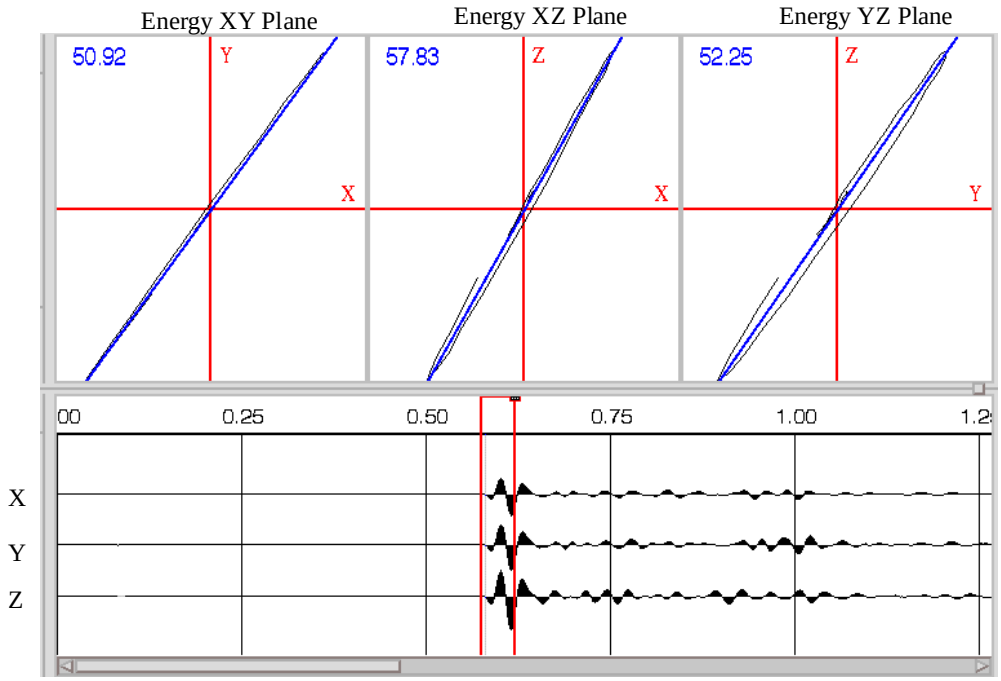

FIG. 6. Hodogram display from source offset –1170 m (west of the observation well). The breakdown of the energy into the XY, XZ, and YZ planes is at the top of the figure. The raw x, y, and z components can be seen below the energy planes. The red window around the first arrivals is the window used for the hodogram analysis.

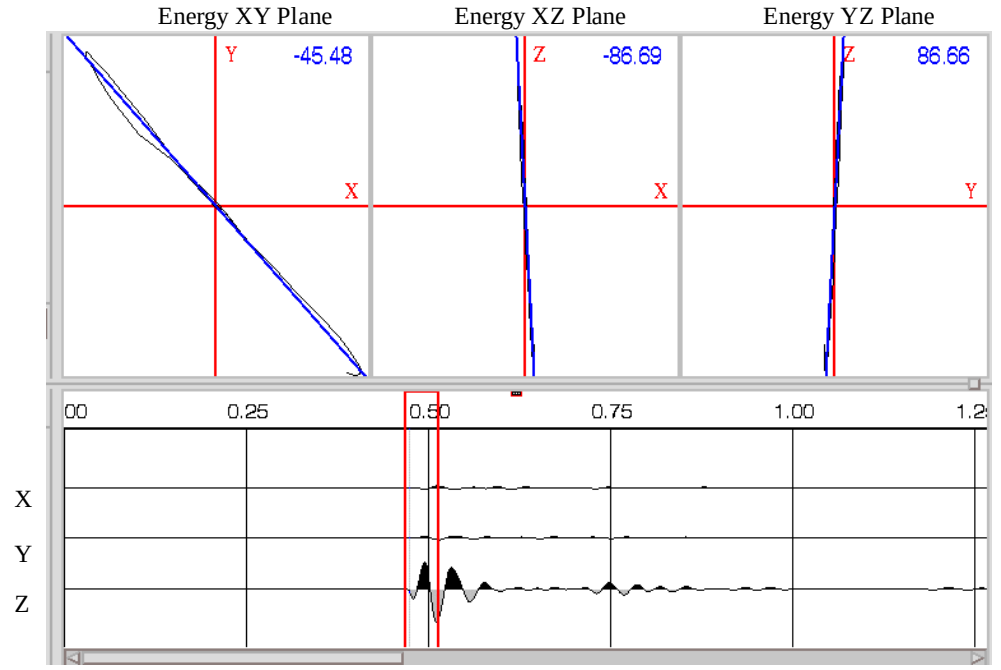

FIG. 7. Hodogram display from the source closest to zero offset.

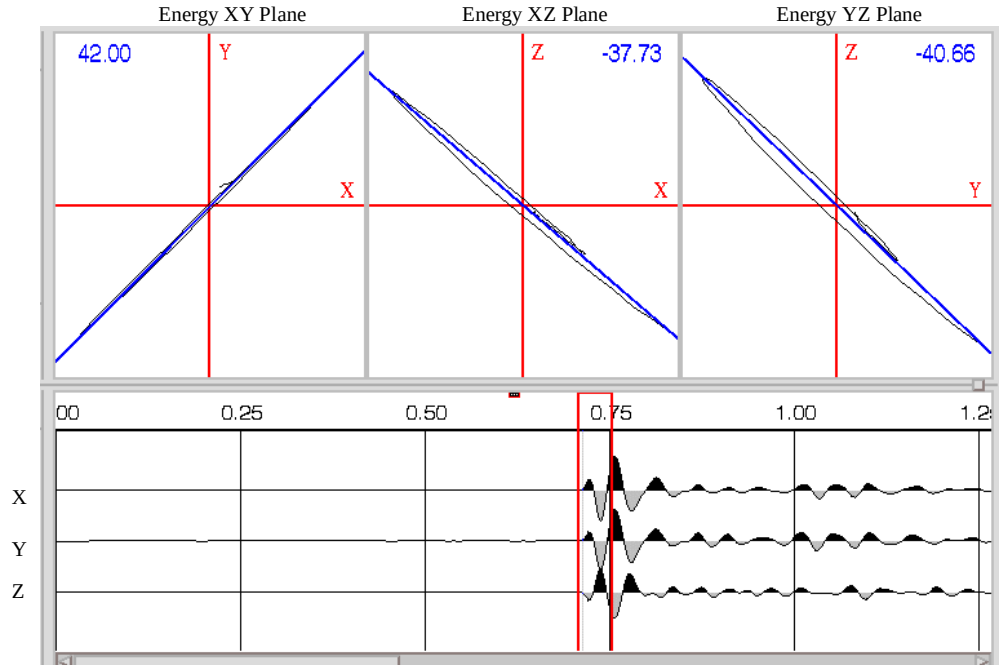

FIG. 8. Hodogram display from source offset 1788 m (east of the observation well).

The data rotation projects the x and y components of the data onto a vector in the vertical plane containing the source and receiver. The rotation analysis is completed for each source-receiver pair. The resulting output is a maximum horizontal component (HMX) that is in the source-receiver plane (Figure 9), and a minimum horizontal component (HMN) that is perpendicular to the HMX wavefield.

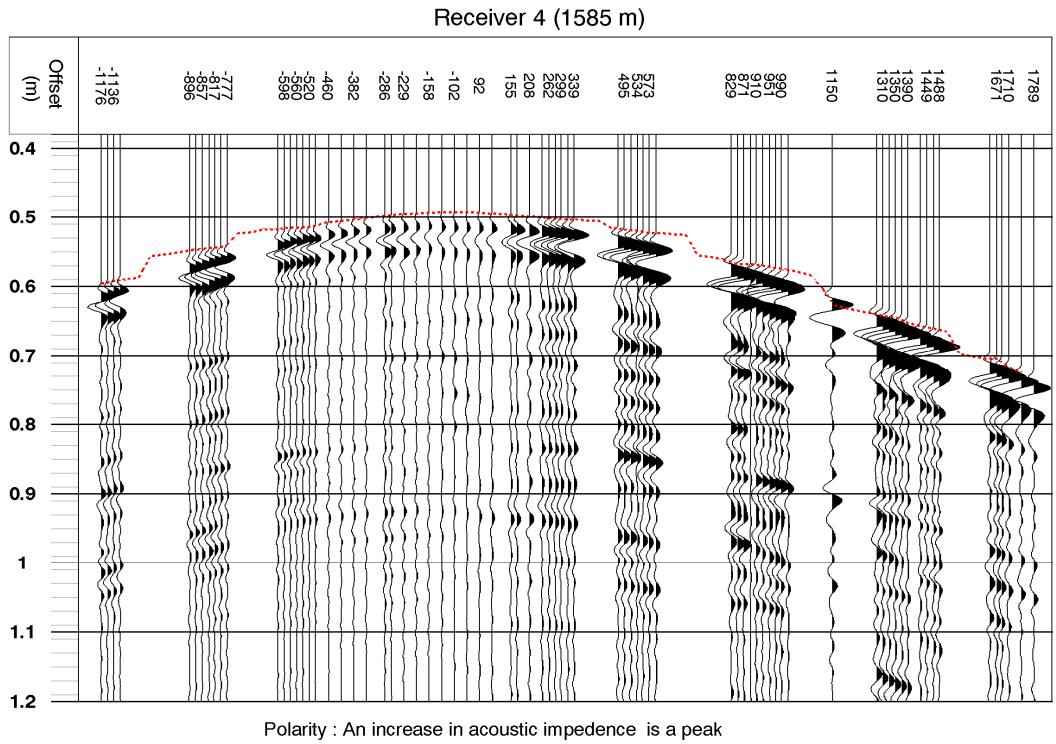

FIG. 9. HMX wavefield output from the polarization analysis.

Wavefield Separation

The downgoing and upgoing wavefields were separated using a velocity model based parametric wavefield decomposition (Leaney and Esmersoy, 1990). This method uses a velocity model, and the HMX and z components to decompose the data into compressional and shear wavefields.

The P-wave and S-wave sonic logs from a nearby production well were used to build an initial velocity model. The closest density log available was from a production well approximately 1.7 km from the observation well and could not easily be correlated to the logs from the nearby production well. Ultimately, a density log was generated using the P-wave velocities and Gardner's equation. A travel time inversion was performed on the model to minimize the difference between the modeled and measured direct arrival times.

The wavefield separation used a 5 level filter with a frequency range of 8 to 100 Hz. Figures 10 through 13 respectively show the downgoing compressional, downgoing shear, upgoing compressional, and upgoing shear at a range of offsets across the line. Each offset has been gather normalized and displays true relative amplitudes. The parametric decomposition is modeling all of the wavefields well at all offsets.

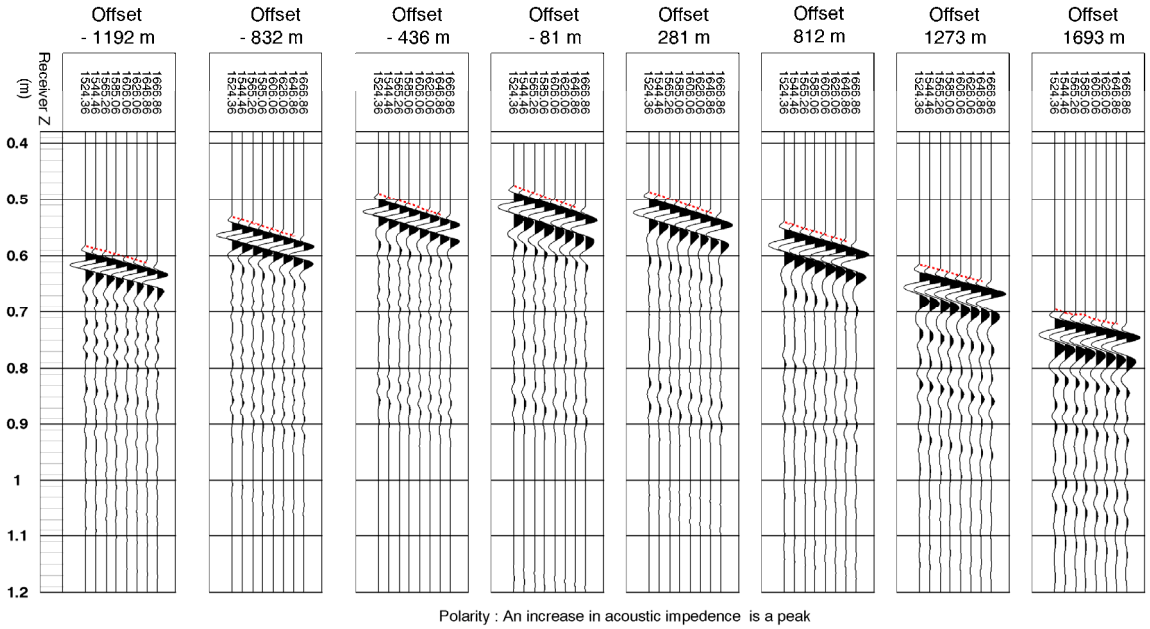

FIG. 10. Downgoing compressional wavefield at varying offsets.

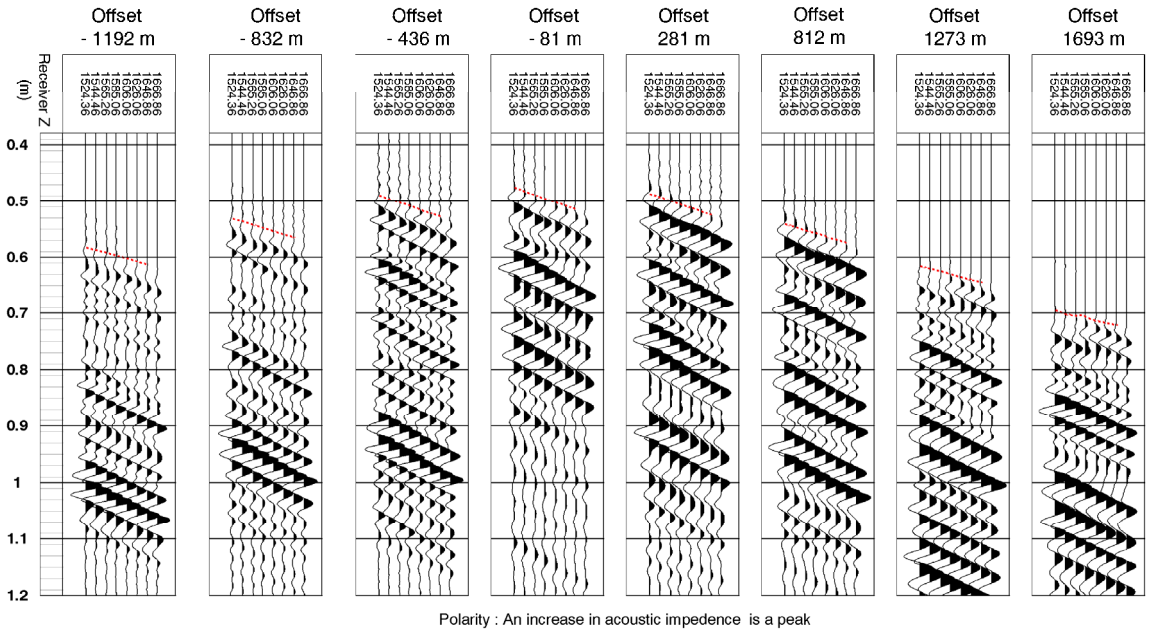

FIG. 11. Downgoing shear wavefield at varying offsets.

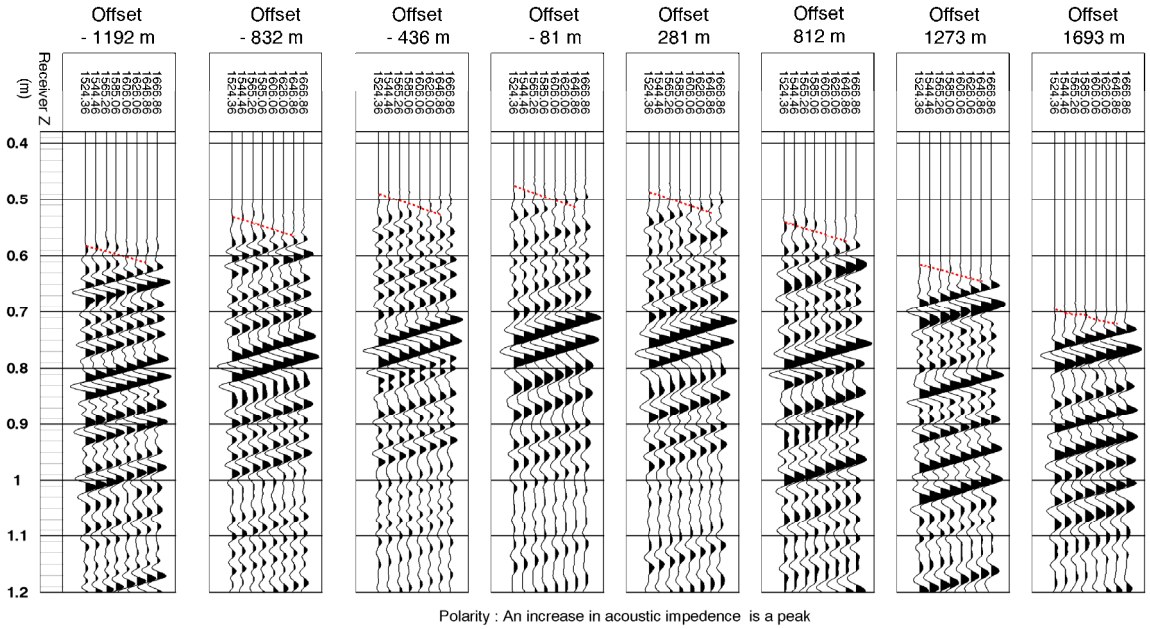

FIG. 12. Upgoing compressional wavefield at varying offsets.

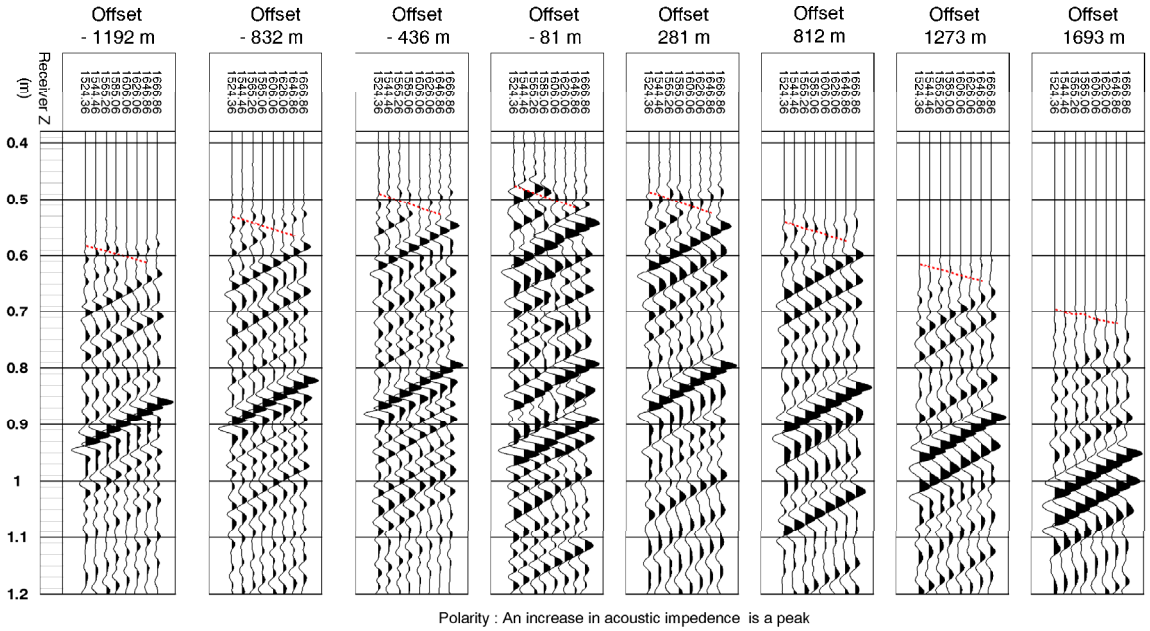

FIG. 13. Upgoing shear wavefield at varying offsets.

Deconvolution

A waveshape deconvolution operator was designed on the downgoing wavefield and applied to the upgoing wavefield. The deconvolution operator collapses the downgoing wavefield to a single spike and allows multiples to be removed from the upgoing wavefield. The deconvolution operator for the PS upgoing wavefield was also designed using the downgoing P-wavefield because the direct P-wave arrivals convert to PS-waves at multiple horizons.

The compressional wavefield was deconvolved using a frequency range from 8 to 90 Hz while the shear wavefield was deconvolved using a frequency range from 8 to 60 Hz. A window of 1.0 s and 1% whitening was used in the deconvolution process. Both upgoing wavefields were muted before the first breaks and resampled to 2 ms prior to migration. Figures 14, 15, and 16 display the deconvolved downgoing wavefield, the upgoing P-wavefield, and the upgoing PS-wavefield respectively.

Note the decrease in PS-wave amplitudes at the near offsets (Figure 16). This is expected as the hodogram analysis showed that the near offsets contained very little shear energy (Figure 7).

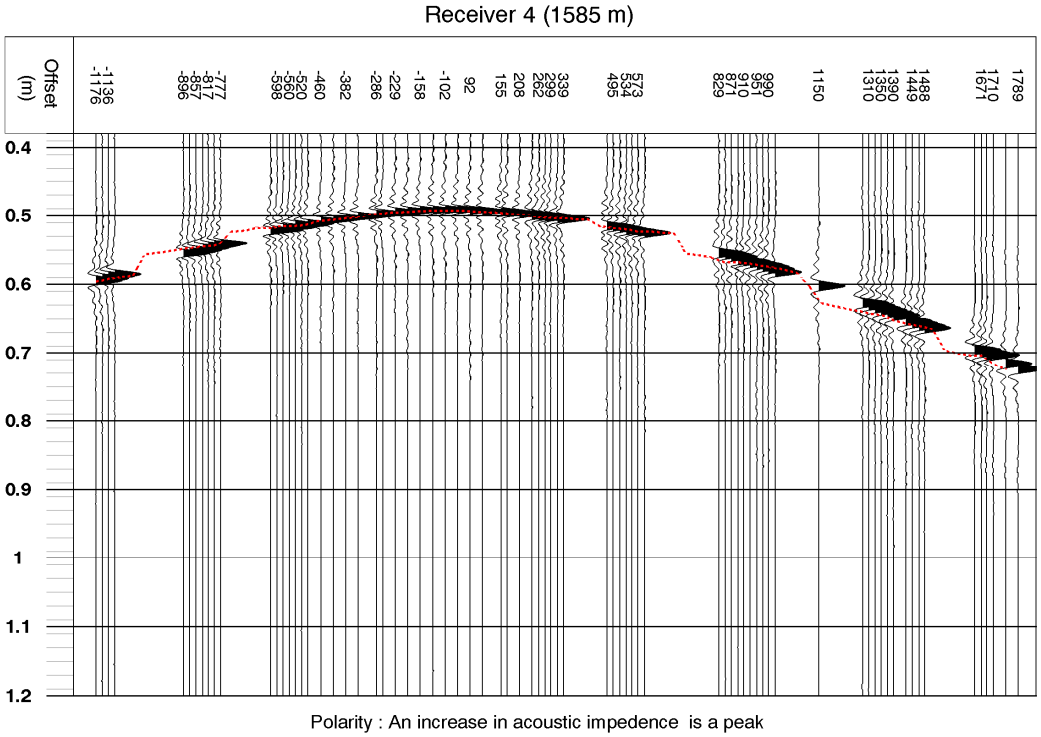

FIG. 14. Deconvolved downgoing P-wavefield (8-90 Hz).

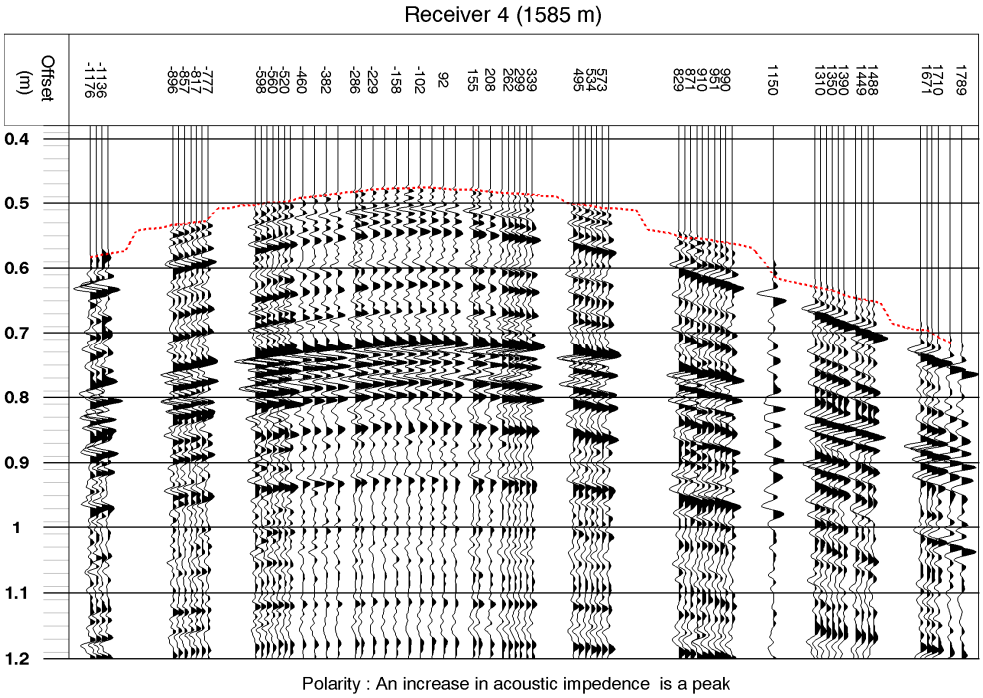

FIG. 15. Deconvolved upgoing P-wavefield (8-90 Hz).

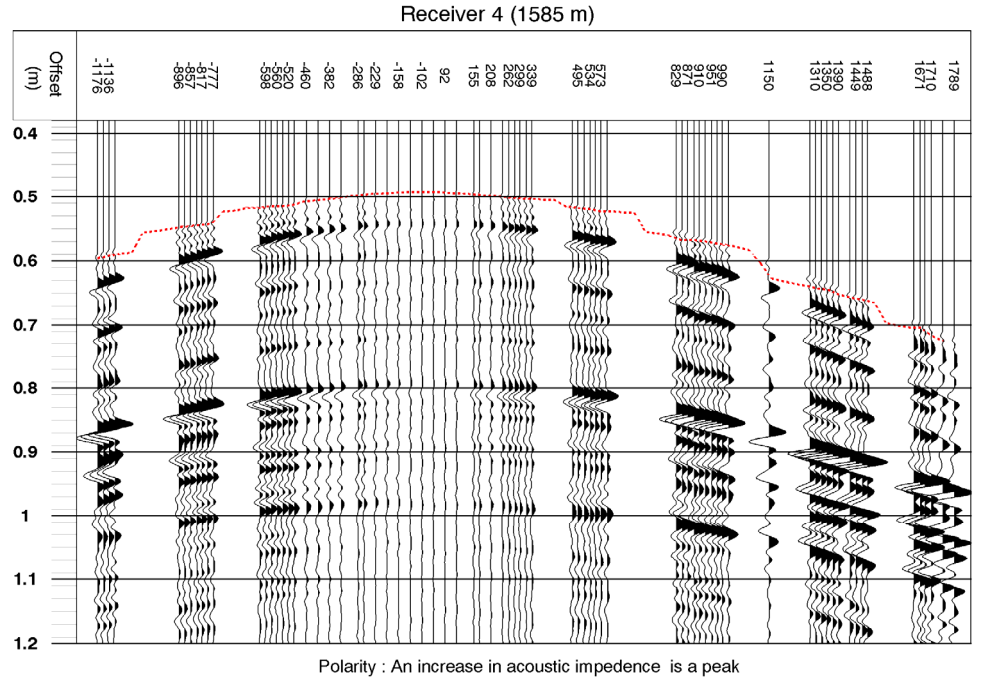

FIG. 16. Deconvolved upgoing S-wavefield (8-60 Hz).

Imaging Velocity Model

The velocity model built for the wavefield separation was not detailed enough to image the data and produce flat horizons. When this velocity model was used to image the data, the shallow horizons showed significant structure that was not seen in surface seismic and did not seem reasonable based on what is known about the geology in the area.

A finely layered velocity model was created – again using the sonic logs from the nearby production well. This time, the zero offset VSP travel times were used to calibrate the P-wave sonic so that corrected velocities were used in the model. The model was then inverted for anisotropy. Anisotropy was allowed to increase linearly with overburden depth, thus honouring the assumption that anisotropy increases with increasing compaction.

The travel time residuals before and after inversion can be seen in Figure 17. Prior to inversion, the residuals times were around zero at the near offsets but quickly increased with increasing offset from the observation well. After inversion, the time residuals vary from zero to a maximum of 3 ms for the whole line.

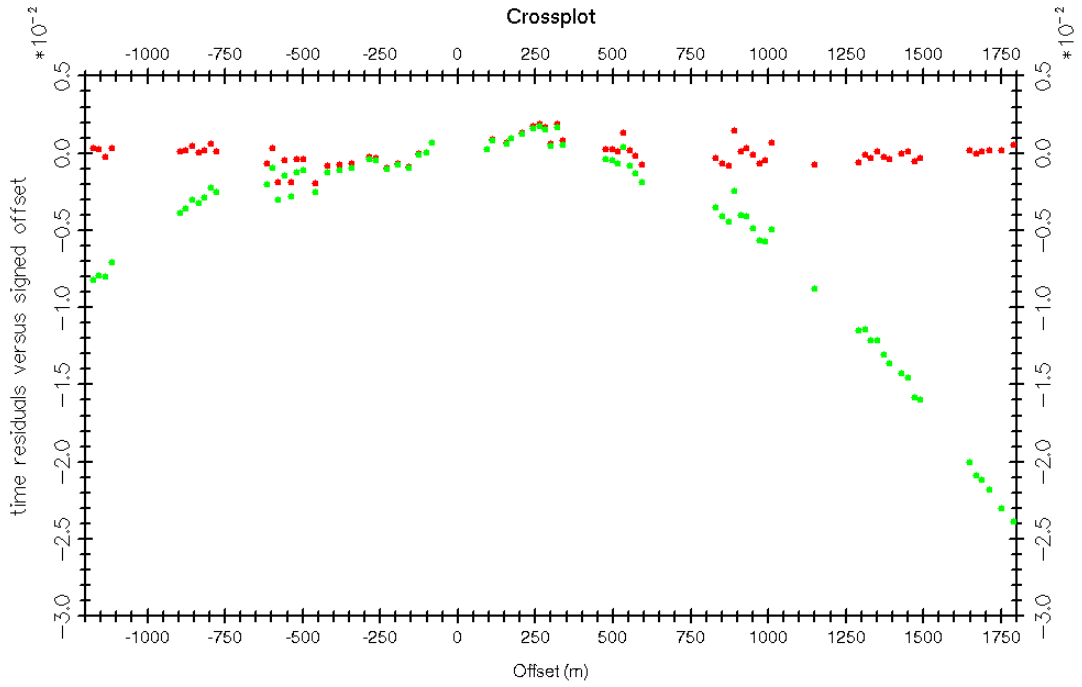

FIG. 17. Residual travel times (ms) versus offset for the migration velocity model before (green dots) and after (red dots) inversion for anisotropy.

Below TD, the P- and S- wave velocities were allowed to increase slowly with depth. A V_P/V_S ratio of 1.8 was used as testing proved that it produced the best tie between the P-wave and S-wave migrations.

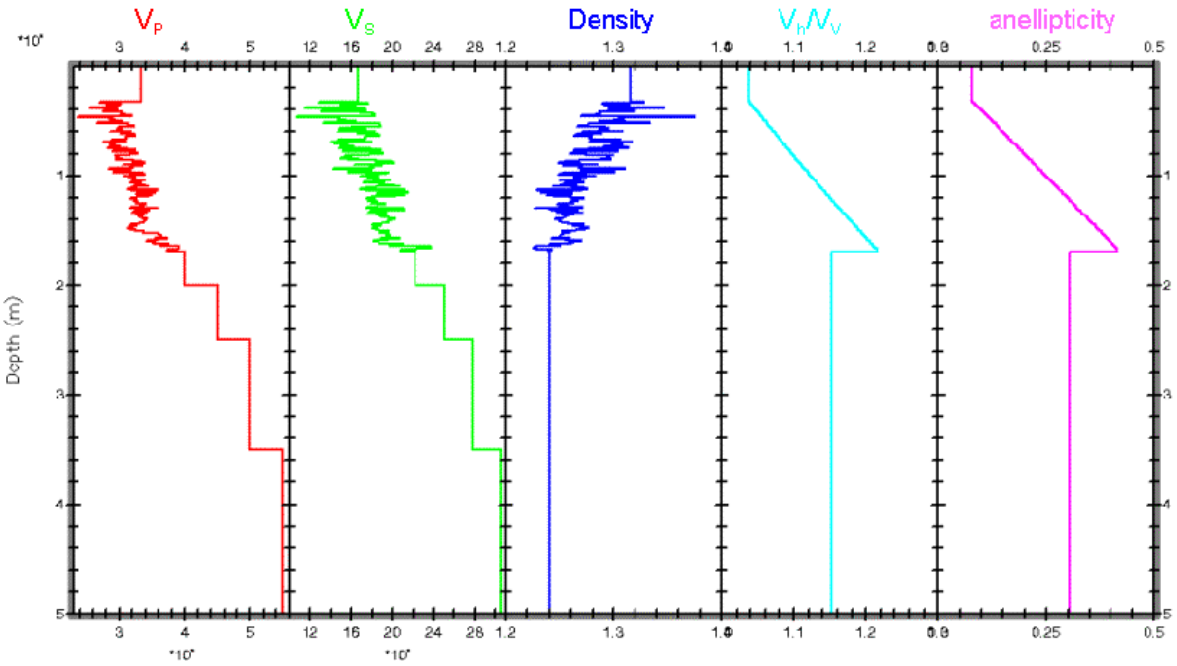

FIG. 18. Anisotropic velocity model used for the VSP migration.

CDP Mapping and Migration

The common depth point (CDP) mapping process places the seismic traces at the correct spatial position and should be similar to a migration with a 1^o aperture. The data was mapped from offsets –500 to 800 m using an increment of 5 m and from 0.5 to 2.5 s using a time increment of 0.001 s. Figure 19 displays the tie between the P-wave CDP map and the corresponding surface seismic.

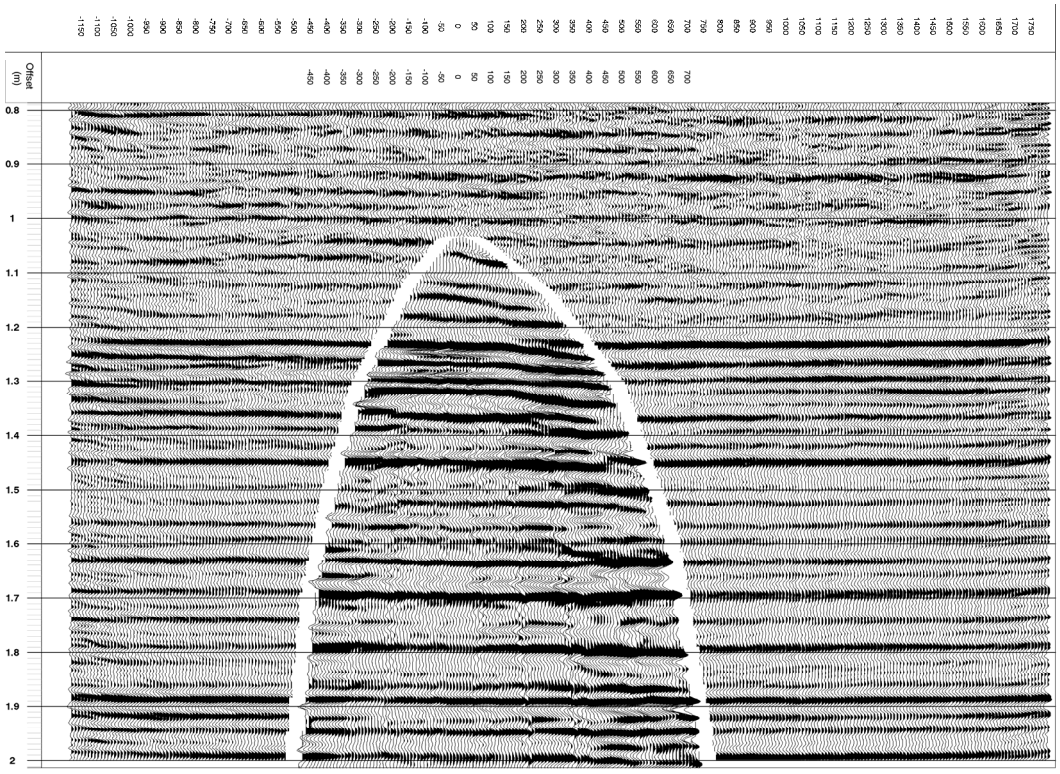

FIG. 19. The CDP map in time tied to the corresponding surface seismic data.

A 1D anisotropic Kirchhoff migration algorithm was used to migrate the P- and PS-wavefields in time. The data was migrated from 0.5 to 2.5 s using a time increment of 4 ms. Spatially, the data was migrated from – 1000 to 1000 m around the observation well using an increment of 5 m. An aperture of 5^o was used for all of the migrations.

Figure 20 shows the tie between the P-wave surface and borehole seismic. The VSP data has been displayed using the same trace spacing as the surface seismic for a more equal comparison. The events in the VSP data tie well with the surface seismic; however, the VSP exhibits greater vertical and lateral resolution than the surface seismic. Even though there are only 8 receivers in the monitor well, at TD the VSP data is imaging an area extending 200 m around the observation well.

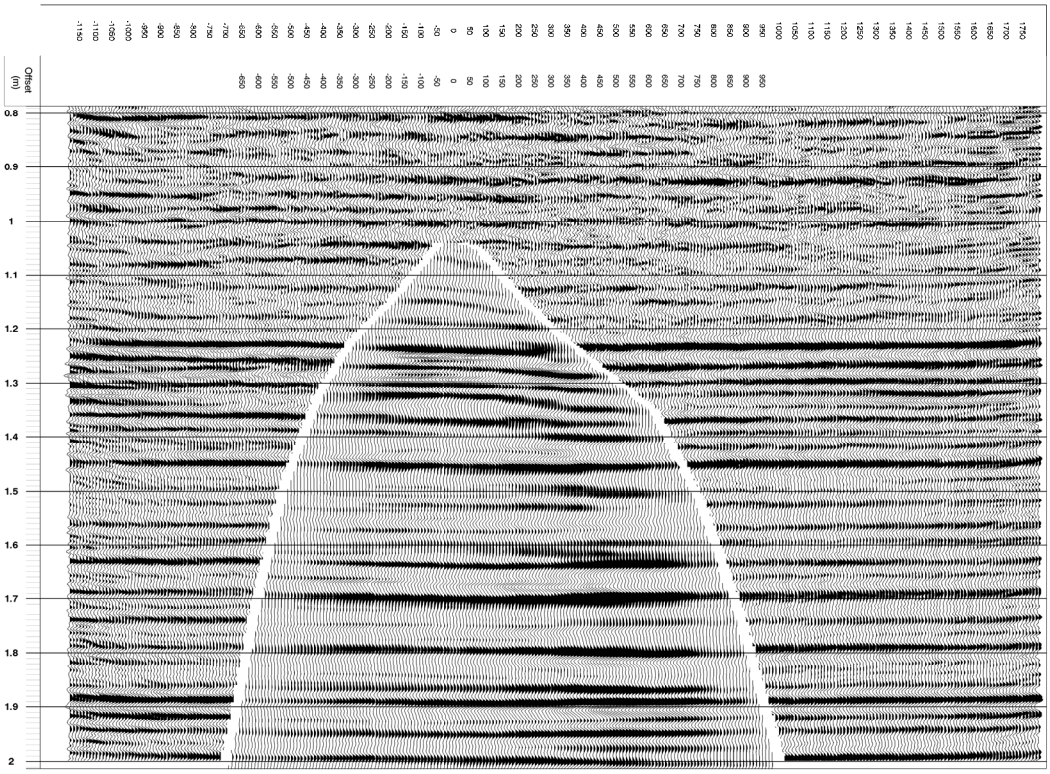

FIG. 20. Tie between the P-wave surface seismic and VSP images.

The PS-wave data was migrated and converted directly into P-wave time so that it could be compared to the P-wave images. The tie between the P-wave surface seismic and the PS-wave VSP data can be seen in Figure 21. The sudden decrease in amplitude near the observation well is related to the lack of shear wave information at the near offsets. The PS-wave events can be clearly tied to events on the P-wave surface seismic. Some of the events on the PS-wave image show more detail than the image from the P-wave VSP. For instance, the events at 1.45 and 1.5 s on the PS-wave image show greater detail and resolution than the corresponding events on the P-wave image.

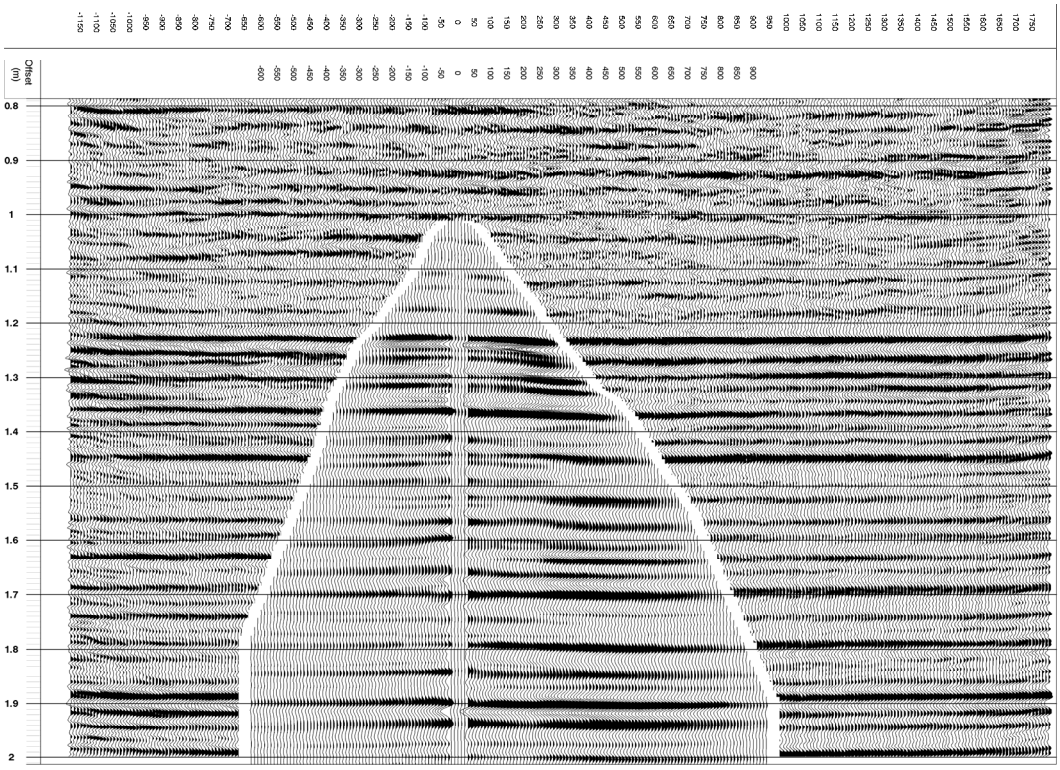

FIG. 21. Tie between the P-wave surface seismic and the migrated S-wave VSP data.

The PS-wave surface seismic was converted to P-wave time using the migration velocity model so that it could be compared to the PS-wave VSP image (Figure 22). The tie here is much less obvious due to the poorer quality of the PS-wave surface seismic data. Much more confidence can be placed on the PS-wave VSP image because of its evident ties with the P-wave VSP image and P-wave surface seismic. In addition, the shear velocity model used to converted the PS-wave surface seismic was not the velocity model used to process the surface seismic, so the time tie with the PS-wave VSP data is not absolute.

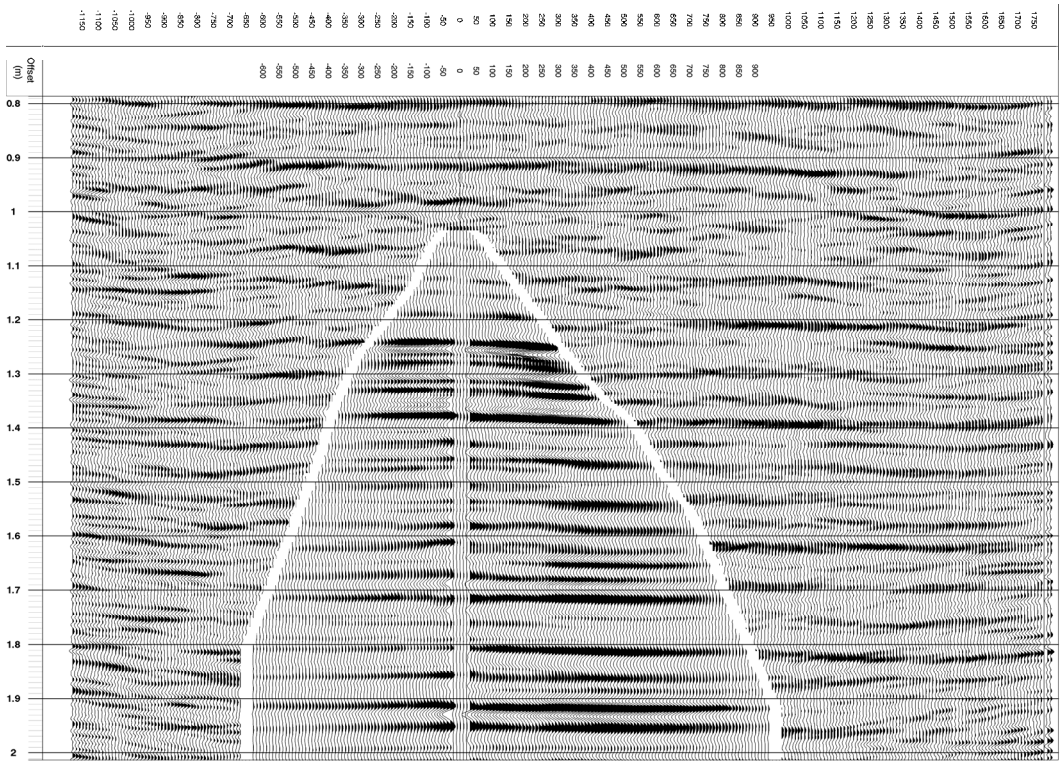

FIG. 22. Tie between the S-wave surface seismic and the migrated S-wave VSP data in P-wave time.

The amplitude spectrum of the zero offset trace was produced for the surface seismic and VSP data (Figure 23). The amplitude spectrum from the VSP data displays good frequencies up to 90 Hz. At first glance, the surface seismic data appears to have a useable frequency range up to 110 Hz. However, the amplitude spectrum has a less consistent shape, and a filter test showed that the signal between 80-110 Hz did not contain useful signal (Figure 24).

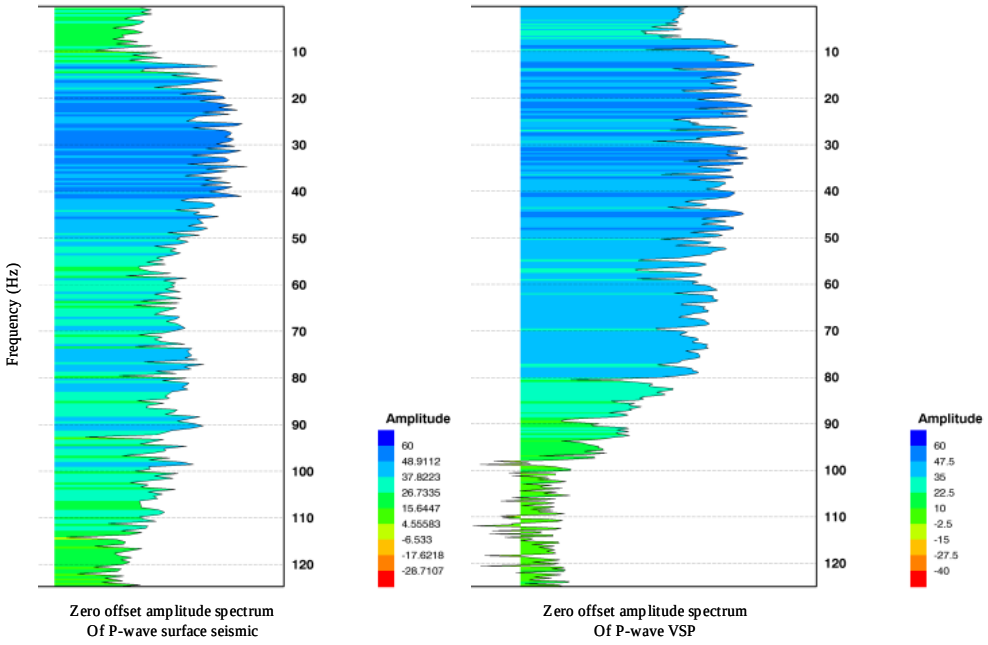

FIG. 23. Comparison of the amplitude spectra (in dB) of the zero offset trace from the P-wave surface seismic (left) and the migrated P-wave VSP data (right).

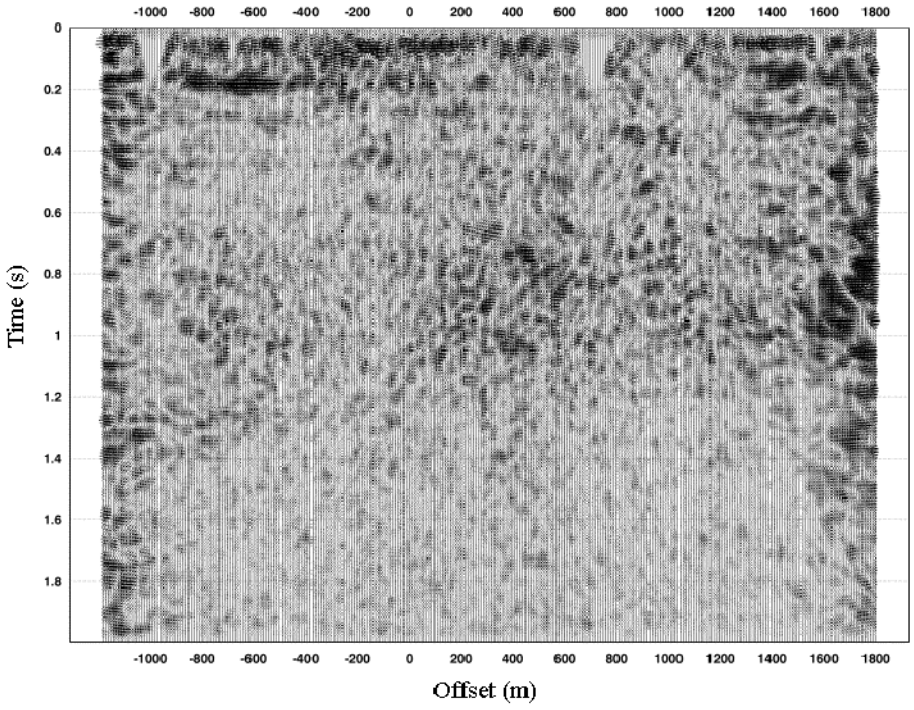

FIG. 24. P-wave surface seismic filter panel from 80-110 Hz.

The amplitude spectra were also generated for the zero offset traces from the S-wave surface seismic and PS-wave VSP data (Figure 25). The PS-wave surface seismic has a frequency range of about 5 to 65 Hz while the PS-wave VSP data has a frequency range of about 8 to 80 Hz. It does not appear that any whitening was applied to the PS-wave surface seismic. The original P-wave amplitude spectrum probably had a similar shape.

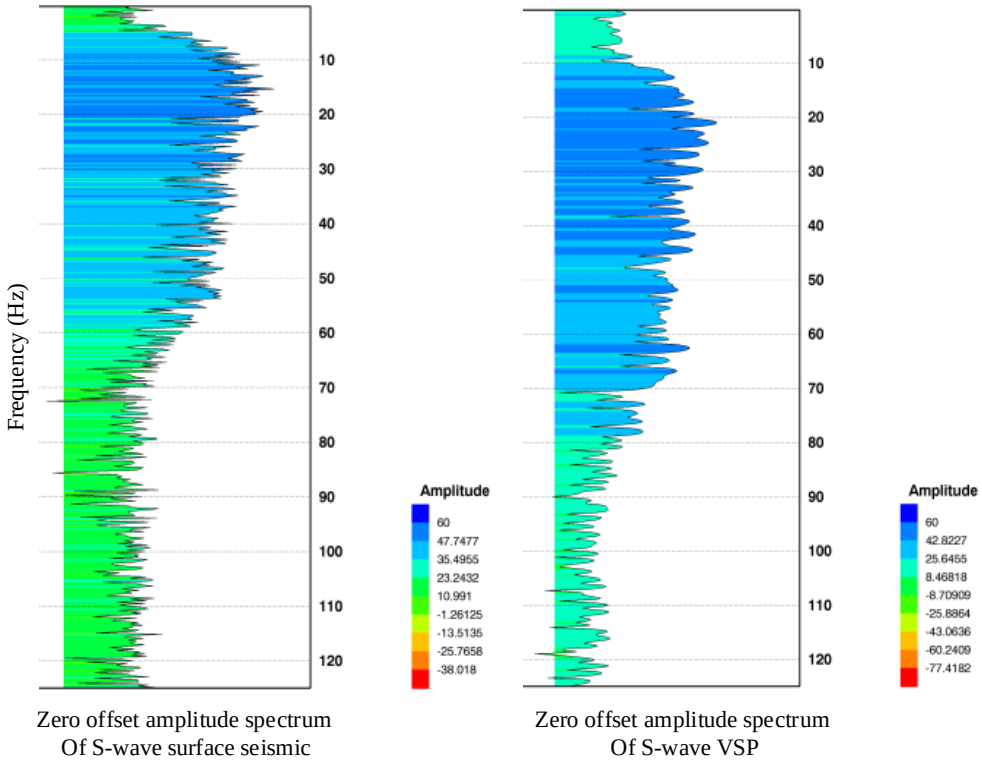

FIG. 25. Comparison of the amplitude spectra (in dB) of the zero offset trace from the S-wave surface seismic (left) and the migrated S-wave VSP data (right).

CONCLUSIONS

The parametric wavefield decomposition was very successful at separating the wavefields. In general, one would expect the process to have problems modeling the shear wavefields at the near offsets, and to have more problems with the compressional wavefields at the far offsets. However, the separations are clean for all of the wavefields at all offsets.

The VSP data has an excellent signal to noise ratio and images reflectors for a radius of approximately a 200 m radius around the observation well. The frequency bandwidth of the P-wave migration is about 8 to 90 Hz, and the PS-wave migration has a frequency content of about 8 to 80 Hz.

The migrated P-wave and PS-wave VSP images tie the P-wave surface seismic data very well. As expected, the VSP images show increased vertical and lateral resolution as compared to the surface seismic data. The PS-wave VSP tie to the PS-wave surface seismic data is less certain; however, this is due to the poor quality of the PS-wave surface seismic data. The VSP migrations also clearly image the Cardium Formation at the top of the VSP section. This is promising as we hope to see progressive changes in the Cardium response with subsequent time-lapse surveys.

FUTURE WORK

AVO analysis will be completed for the Cardium Formation using the borehole seismic data. The predicted AVO response of the Cardium will also be modeled using the well logs from the nearby production well for comparison to the borehole seismic data.

The first monitor survey is scheduled to be acquired in January 2006. The new borehole seismic data will be processed using the same parameters as the baseline survey. The goal will be to identify differences between the monitor survey and the baseline data so that changes caused by the CO_2 flood can be identified. The new data will be analyzed for any changes in its AVO response as well. Based on similar experiments, such as the Weyburn Field in Saskatchewan, the first monitor survey should display decreased P-wave velocities, and increased reflection impedance and travel times in the areas inundated by CO_2 (Li, 2003).

ACKNOWLEDGEMENTS

We would like to thank:

Schlumberger Data and Consulting Services for allowing one of us to use their resources while working on a thesis.

Alberta Energy Research Institute (AERS)

Western Economic Diversification (WED)

CREWES for its continued financial support.

PennWest Petroleum

REFERENCES

Bachu, S., and Shaw, J.C., 2004, CO_2 storage in oil and gas reservoirs in Western Canada: effect of aquifers, potential for CO_2-Flood enhanced oil recovery and practical capacity: GHGT-7.

Leaney, W. S. P., and Esmersoy, C., 1989, Parametric decomposition of offset VSP wave fields: SEG Technical Program Expanded Abstracts **9**, 1097-1100.

Li, G., 2003, 4D seismic monitoring of CO_2 flood in a thin fractured carbonate reservoir: The Leading Edge, **22**, 690-695.

O'Brien, J., Kilbride, F., and Lim, F., 2004, Time-lapse 3-D VSP monitoring of a CO_2 EOR Flood: SEG Technical Program Expanded Abstracts **23**, 2267-2270.

Skov, T., Borgos, H. G., Halvorsen K. Å. Randen, T., Sønneland,, L., Arts, R., and Chadwick, A., 2002, Monitoring and characterization of a CO_2 storage site: SEG Technical Program Expanded Abstracts **21**, 1669-1672.